



CHORUS

This is the accepted manuscript made available via CHORUS. The article has been published as:

Theoretical and experimental investigation of the equation of state of boron plasmas

Shuai Zhang, Burkhard Militzer, Michelle C. Gregor, Kyle Caspersen, Lin H. Yang, Jim Gaffney, Tadashi Ogitsu, Damian Swift, Amy Lazicki, D. Erskine, Richard A. London, P. M. Celliers, Joseph Nilsen, Philip A. Sterne, and Heather D. Whitley

Phys. Rev. E **98**, 023205 — Published 23 August 2018

DOI: [10.1103/PhysRevE.98.023205](https://doi.org/10.1103/PhysRevE.98.023205)

Theoretical and experimental investigation of the equation of state of boron plasmas

Shuai Zhang,^{1,*} Burkhard Militzer,^{2,3,†} Michelle C. Gregor,^{1,‡} Kyle Caspersen,¹ Lin H. Yang,¹ Jim Gaffney,¹ Tadashi Ogitsu,¹ Damian Swift,¹ Amy Lazicki,¹ D. Erskine,¹ Richard A. London,¹ P. M. Celliers,¹ Joseph Nilsen,¹ Philip A. Sterne,¹ and Heather D. Whitley^{1,§}

¹*Lawrence Livermore National Laboratory, Livermore, California 94550, USA*

²*Department of Earth and Planetary Science,*

University of California, Berkeley, California 94720, USA

³*Department of Astronomy, University of California, Berkeley, California 94720, USA*

(Dated: August 6, 2018)

Abstract

We report a theoretical equation of state (EOS) table for boron across a wide range of temperatures (5.1×10^4 – 5.2×10^8 K) and densities (0.25–49 g/cm³), and experimental shock Hugoniot data at unprecedented high pressures (5608 ± 118 GPa). The calculations are performed with first-principles methods combining path integral Monte Carlo (PIMC) at high temperatures and density functional theory molecular dynamics (DFT-MD) methods at lower temperatures. PIMC and DFT-MD cross-validate each other by providing coherent EOS (difference < 1.5 Hartree/boron in energy and $< 5\%$ in pressure) at 5.1×10^5 K. The Hugoniot measurement is conducted at the National Ignition Facility using a planar shock platform. The pressure-density relation found in our shock experiment is on top of the shock Hugoniot profile predicted with our first-principles EOS and a semi-empirical EOS table (LEOS 50). We investigate the self diffusivity and the effect of thermal and pressure-driven ionization on the EOS and shock compression behavior in high pressure and temperature conditions. [We also study the sensitivity of a polar direct-drive exploding pusher platform to pressure variations based on applying pressure multipliers to LEOS 50 and by utilizing a new EOS model based on our *ab initio* simulations via 1D radiation-hydrodynamic calculations.](#) The results are valuable for future theoretical and experimental studies and engineering design in high energy density research.

* zhang49@llnl.gov

† militzer@berkeley.edu

‡ gregor3@llnl.gov

§ whitley3@llnl.gov

11 I. INTRODUCTION

12 Recent experiments at the National Ignition Facility (NIF) have demonstrated the utility
13 of large diameter polar direct-drive exploding pushers (PDXP) as a low areal density plat-
14 form for nucleosynthesis experiments [1], neutron source development, neutron and x-ray
15 diagnostic calibration, and potentially as a candidate platform for heat transport studies [2].
16 Improving the platform for each of these respective uses requires consideration of various
17 model uncertainties. Achieving a lower shell areal density during burn or obtaining addi-
18 tional data to help constrain estimates of this quantity in the nucleosynthesis experiments
19 would simplify analysis of the charged particle data collected, while improving implosion
20 symmetry is a necessary requirement if the platform is to be used to study heat transport.
21 Variations in the ablators used in these experiments is one possible avenue that is currently
22 under investigation. The use of glow-discharge polymer (GDP) as an ablator improves per-
23 formance over smaller glass capsules [1], but its low tensile strength requires designs with
24 shell thickness of about 15-20 μm in order to support gas fill pressures of around 8 bar.
25 Higher tensile strength materials offer the option of producing thinner shells to support
26 similar fill pressures, and reactions of ablator materials with neutrons and protons could
27 potentially be used to obtain additional data to help quantify shell areal density at burn
28 time. Some candidate materials with higher tensile strength include beryllium, boron, boron
29 carbide, boron nitride, and high density carbon. For the purpose of conducting heat flow
30 measurements, beryllium was ruled out as a candidate material due to the inclusion of ar-
31 gon within the capsule during the fabrication process [2]. Boron and nitrogen, which both
32 undergo reactions with neutrons and protons, offer the potential for using additional nuclear
33 reactions to better constrain the shell areal density during nuclear burn time, which could
34 improve our overall understanding of the effects of the shell on the measured charged par-
35 ticles in the nucleosynthesis experiments. Boron is also interesting as an ablator material
36 since its reactions with γ -rays could be used to constrain ablator mix at burn time.[3]

37 Radiation hydrodynamic simulations are the workhorse method for design and analy-
38 sis of the inertial confinement fusion (ICF) and high energy density experiments. It has
39 been demonstrated in many previous studies that the equation of state (EOS) of capsule
40 ablator materials is an important component in indirect drive ICF performance [4–8], and
41 EOS may also affect the implosion dynamics in the polar direct-drive platform, impacting

42 not only capsule yield, but also the shell areal density during burn and the electron-ion
43 temperature separation in the gas. Thus, exploration of these materials as candidates for
44 future PDXP-based experiments requires reasonable EOS models for use in radiation hy-
45 drodynamic simulations. In this paper, we examine the EOS of boron via both *ab initio*
46 simulations and experimental measurements. We also examine its performance as an ablator
47 in 1D simulations of the PDXP platform, focusing on how variations in the EOS impact the
48 computed yield and plasma conditions at burn time.

49 EOS models that are widely used in hydrodynamic simulation codes, such as the quotidian
50 EOS (QEOS) [9, 10], provide pressures and energies as smooth functions of temperature and
51 density based on semi-empirical methods, such as the Thomas-Fermi (TF) theory. The TF
52 theory treats the plasma as a collection of nuclei that follow Boltzmann statistics and elec-
53 trons that form continuous fluids and obey Fermi-Dirac statistics. This offers a good means
54 to describe weakly-coupled plasmas and materials at very high densities, but is insufficient in
55 describing many condensed matter solids and liquids, where bonding effects are significant.
56 Additionally, at low-to-intermediate temperatures where atoms undergo partial ionization,
57 the TF theory does not accurately capture the effects of shell ionization, which impacts the
58 electronic contribution to the EOS of the material.

59 There has been continuous research in the development of improved methods for com-
60 puting thermodynamic properties of materials, which has resulted in a variety of methods
61 that can be applied to study EOS across a wide range of densities and temperatures. [Several density functional theory \(DFT\)-based methods are appropriate to the study of dense
62 plasmas, such as INFERNO \[11\], Purgatorio \[12, 13\], orbital-free \(OF\) quantum molecular
63 dynamics \(MD\) \[14, 15\], and extended-DFT \[16\]. Standard Kohn-Sham DFT-MD \[17–19\]
64 has been widely applied for EOS studies of condensed matter as well as warm and hot, dense
65 plasmas. It accounts for both the electronic shells and bonding effects, and is thus superior
66 to average-atom methods in situations where these types of strong many-body correlations
67 are impactful to the EOS. However, the DFT-MD approach becomes computationally in-
68 tractable at high temperatures because considerable numbers of partially occupied orbitals
69 need to be considered. \[Other noteworthy approaches for plasmas and warm-dense mat-
70 ter EOS research include the activity-expansion method \\(ACTEX\\) \\[20–22\\] and many-body
71 quantum Monte Carlo methods \\[23–29\\].\]\(#\)](#)

72 In ACTEX calculations, the plasma grand partition function is expanded as a series of
73

74 terms describing the interactions between increasingly large numbers of fundamental plasma
75 particles (electrons and boron nuclei in this case) [30, 31]. Screened interactions and electron
76 bound states arise naturally through a set of resummations, resulting in a convergent series
77 which explicitly describes the formation of ions and molecules as well as quantum mechanical
78 corrections to the EOS [32, 33]. After resummation, electron-ion bound states are described
79 in terms of their internal (Planck-Larkin) partition function which allows detailed atomic
80 structure to be included in the EOS. This allows a clear link with other plasma microphysics
81 quantities such as opacity, and ACTEX calculations are an important component of OPAL
82 plasma opacity calculations [34]. ACTEX calculations, and OPAL opacities, have been
83 extensively checked and found to be reliable even for quite strongly coupled plasmas [35].
84 The increasing complexity of terms as the number of interacting particles increases means
85 that only the first few terms in the expansion are known, effectively limiting the ACTEX
86 approach to high temperatures and moderate densities.

87 As a powerful tool initially developed for hydrogen [36], path integral Monte Carlo
88 (PIMC) has been successfully utilized to study plasmas from weak coupling to strongly
89 coupled regimes with high accuracy. Recent developments by Militzer et al. [27, 37] provide
90 useful recipes for studying higher-Z plasmas. In the past seven years, they have imple-
91 mented the PIMC methods under the fixed-node approximation [38] and obtained the EOS
92 for a series of elements (C, N, O, Ne, Na, Si) [27, 37, 39–43] and compounds (H₂O, LiF,
93 hydrocarbons) [37, 44–46] over a wide range of temperature, pressure conditions. The goal
94 of the theoretical part of this paper is to apply these methods to calculate the EOS of boron,
95 and explore the effect on PDXP simulations in comparison with an older EOS model (LEOS
96 50) through hydrodynamic simulations.

97 Located in between metals and insulators in the periodic table, the structure and proper-
98 ties of boron have attracted wide interest in high pressure physics. A number of studies have
99 examined the stability relations of the α and the β phases [47–50], structural complexity
100 of the β -rhombohedral phase [51, 52], and phase transformation and melting of different
101 boron polymorphs in high-pressure, temperature conditions [53–58]. A phase diagram was
102 proposed [59] based on theoretical and experimental studies at up to 300 GPa and showed
103 five different crystalline phases, among which the α -Ga phase has not been experimentally
104 verified so far [60]. There are experimental evidence for the existence of other phases (α , β , γ ,
105 and t), although questions remain on the exact phase boundary and the crystal structure of

106 the t phase [52, 60].

107 A considerable amount of study has been performed on boron at low densities, including
108 DFT-MD simulations and X-ray radiography measurements on the structure, electronic,
109 and thermodynamic properties of liquid boron [61, 62], general chemical models for the
110 the composition and transport properties of weakly-coupled boron plasmas [63], isochoric
111 EOS and resistivity of warm boron by combining closed vessel (EPI) experiments [64–66],
112 DFT-MD [64], average-atom methods [67–69], and a chemical model (COMPTRA) [70].
113 In comparison to the vast progress in the low-temperature, high-pressure and the high-
114 temperature, low-pressure regions of the boron phase diagram, studies at simultaneously
115 high pressures and temperatures are rare. Until the year 2013, the only shock Hugoniot
116 data available were at pressures below 112 GPa [71]. Recently, Le Pape et al. [72] used X-
117 ray radiography to study the structure of shocked boron. They reported two experimental
118 Hugoniot measurements (to the pressure of 400 GPa, which was the highest record to date)
119 and ion-ion structure factors that are consistent with DFT-MD simulations. In this work,
120 we conduct a dynamic compression experiment at NIF and extend the shock Hugoniot
121 measurements of boron to a pressure of 14 times the previous record.

122 Hydrodynamic simulations of PDXP experiments require the EOS of the ablator materi-
123 als along and off the Hugoniot curve at higher temperatures and pressures. The LEOS [9, 10]
124 and SESAME [73] EOS databases may be used, but it is unclear how their deviation from
125 the true values affect the reliability of results in PDXP simulations, such as the neutron
126 yield. In this work, we perform calculations of the boron EOS over a wide range of tem-
127 peratures and pressures. We extend PIMC simulations of dense boron plasmas from the
128 “hot” (weak coupling and degeneracy) down to the “warm” region (coupling parameter and
129 degeneracy both ≈ 1 , see Fig. 1), where significant partial ionization of the K shell persists
130 and standard DFT-MD simulations with frozen 1s core pseudopotential are not trustworthy.
131 At relatively low temperatures, the system behaves like the usual condensed matter fluid,
132 which can be reasonably well described within the DFT-MD framework. By pushing PIMC
133 to low temperatures and DFT-MD to high temperatures, we get a coherent, first-principles
134 EOS table for boron. We compare this table and the predicted shock compression profiles
135 with LEOS and SESAME EOS tables for boron, and perform hydrodynamic simulations to
136 compare the effect of the different tables on the ICF performance.

137 The paper is organized as follows: Section II introduces the details of our simulation

138 methods and experiment. Sec. III presents our EOS results, the calculated and measured
139 shock Hugoniot data, and comparisons with other theories and models. Sec. IV discusses
140 the atomic and electronic properties of boron plasmas, the ionization process, and PDXP
141 performance sensitive to the EOS; finally we conclude in Sec. V.

142 II. THEORY AND EXPERIMENT

143 A. First-principles simulation methods

144 Following the pioneering work applying PIMC to the simulations of real materials (hydro-
145 gen) [36] and recent development for pure carbon [37], hydrocarbons [45, 46], and LiF [44],
146 our PIMC simulations [74] utilize the fixed-node approximation [38] and treat both electrons
147 and the nuclei as quantum paths that are cyclic in imaginary time $[0, \beta=1/k_B T]$, where k_B
148 is the Boltzmann constant. We use free-particle nodes to constrain the path to positive
149 regions of the trial density matrix, which has been shown to work well for calculations of
150 hydrogen [36, 75–82], helium [83, 84], and other first-row elements [37, 39–41, 44]. The
151 Coulomb interactions are described via pair density matrices [85, 86], which are evaluated
152 at an imaginary time interval of $[512 \text{ Hartree (Ha)}]^{-1}$. The nodal restriction is enforced in
153 much smaller steps of $[8192 \text{ Ha}]^{-1}$.

154 For our DFT-MD simulations, we choose the hardest available projected augmented wave
155 (PAW) pseudopotential [87] for boron with core radii of 1.1 Bohr and frozen $1s^2$ electron, as
156 provided in the Vienna *Ab initio* Simulation Package (VASP) [88]. We use the Perdew-Burke-
157 Ernzerhof (PBE) [89] functional to describe the electronic exchange-correlation interactions,
158 [which is consistent with previous DFT calculations on solid boron \[90–92\]](#). We choose a large
159 cutoff energy of 2000 eV for the plane-wave basis, and we use the Γ point to sample the
160 Brillouin zone. The simulations are carried out in the NVT ensemble with a temperature-
161 dependent time step of 0.05-0.55 fs, chosen to ensure reasonable conservation of energy. The
162 temperature is regulated by a Nosé thermostat [93]. Each MD trajectory typically consists of
163 5000 steps to ensure that the system has reached equilibrium and to establish convergence
164 of the energies and pressures. DFT-MD energies from VASP reported in this study are
165 shifted by -24.596 Ha/B , the all-electron PBE energy of a single boron atom determined
166 with OPIUM [94], in order to establish a consistent comparison with the all-electron PIMC

167 energies.

168 Our PIMC calculations are performed at temperatures from 5.05×10^5 K to 5.17×10^8
169 K and densities ranging from 0.1- to 20-times the ambient density ρ_0 (~ 2.46 g/cm³ based
170 on that of the α phase [95]). We conduct DFT-MD simulations at temperatures between
171 5.05×10^4 K and 10^6 K, in order to check the PIMC calculations at the lowest temperatures.
172 Due to limitations in applying the plane-wave basis for orbital expansion at low densities,
173 and limitations in the applicability of the pseudopotential that freeze $1s^2$ electrons in the core
174 at high densities, we consider a smaller number of densities (ρ_0 – $10\rho_0$) in DFT-MD. These
175 conditions are relevant to the dynamic shock compression experiments we have conducted
176 at the NIF, and span the range in which Kohn-Sham DFT-MD simulations are feasible. All
177 PIMC calculations use 30-atom cubic cells, while in DFT-MD we consider both 30-atom
178 cells and larger cells with 108 and 120 boron atoms to minimize the finite-size errors.

179 The temperature-density conditions included in this study are show in Fig. 1, along with
180 contour lines corresponding to the ionic coupling parameter, $\Gamma = (Z^*e)^2/(ak_B T)$, and the
181 electron degeneracy parameter, $\Theta = T/T_{\text{Fermi}}$, where T_{Fermi} is the Fermi temperature of
182 free electrons, Z^* is the effective ion charge, k_B is the Boltzmann constant, $a = (3/4\pi n)^{1/3}$
183 is the average ionic distance, and n is the ion number density. Our PIMC and DFT-MD
184 calculations span a wide range of conditions for the boron plasma, including weakly coupled
185 ($\Gamma < 1$) plasmas, as well as collisional, strongly coupled ($\Gamma > 1$) and degenerate ($\Theta < 1$)
186 plasmas. We utilize the simulation data to predict the principal shock Hugoniot profile over
187 a range of pressures spanning 10 to 10^5 megabar (Mbar), as described in Section III B.

188 B. Shock Hugoniot experiment

189 An experiment to measure boron’s Hugoniot near 50 Mbar was done at the NIF [97]
190 at Lawrence Livermore National Laboratory (shot number N170801), using the impedance-
191 matching technique [98]. As shown in Fig. 2, the target physics package was affixed to
192 the side of a gold hohlraum and comprised a 200- μm -thick diamond ablator, 5- μm -thick
193 gold preheat shield, and a 100- μm -thick diamond impedance-matching standard backing
194 individual diamond, boron, and quartz samples. The optical-grade chemical vapor deposition
195 diamond was polycrystalline with a density of 3.515 g/cm³. The z-cut α -quartz and the
196 boron had densities of 2.65 g/cm³ and 2.31 g/cm³, respectively. 176 laser beams in a

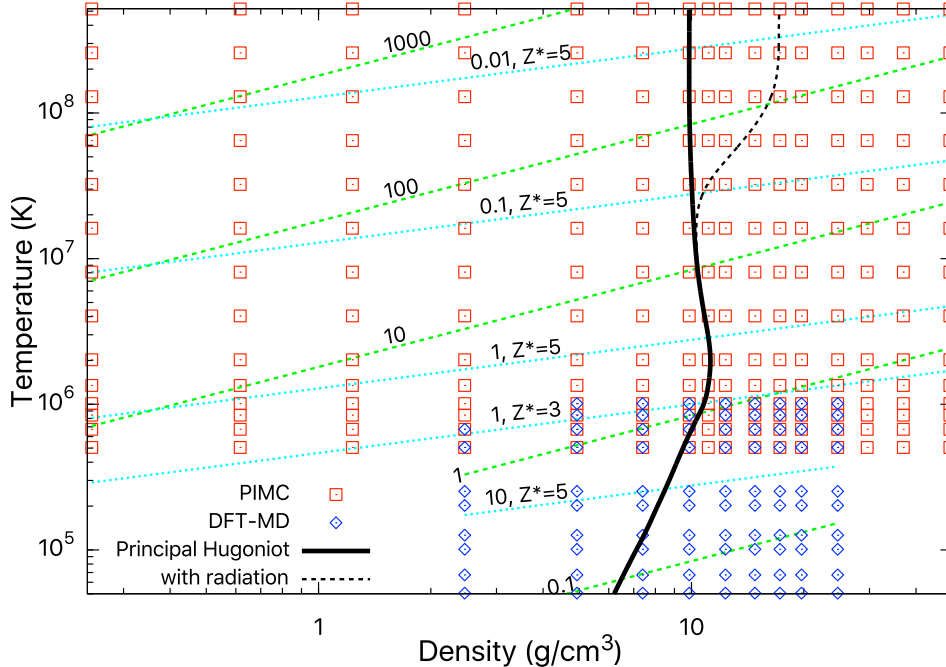


FIG. 1. Temperature-density conditions in our PIMC (red squares) and DFT-MD (blue diamonds) calculations are shown. The black curves depict the computed principal Hugoniot with (dashed) and without (solid) radiation correction [96] to the EOS. The dashed lines in green represent the conditions with different values of the degeneracy parameter, Θ , and the dotted lines in cyan denote the effective ionic coupling parameter, Γ . The Hugoniot curve is constructed by choosing the initial density to be the same as ρ_0 (~ 2.46 g/cm³).

197 5-ns pulse with a total energy of 827 kJ produced an x-ray bath in the hohlraum with
 198 a peak radiation temperature of 250 eV as measured by the Dante multi-channel soft x-
 199 ray spectrometer [99]. The x rays launched a strong, planar and nearly steady shock wave,
 200 shown by measurements using a line-imaging velocity interferometer system for any reflector
 201 (VISAR) to vary $\sim \pm 3\%$ from its average velocity in the boron, that drove the samples to
 202 high pressures and temperatures.

203 The boron Hugoniot measurement was determined by impedance matching using the
 204 inferred shock velocities in the boron sample and diamond standard. Average shock velocities
 205 were determined from shock transit times, measured using VISAR [100], and the initial
 206 sample thicknesses, measured using a dual confocal microscope. The average velocities
 207 were further corrected for shock unsteadiness witnessed *in situ* in the transparent quartz

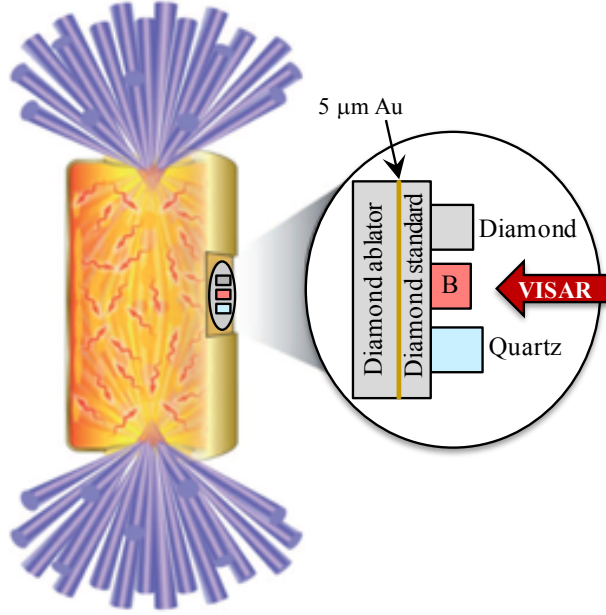


FIG. 2. Target design for the impedance-matching experiment at the NIF.

TABLE I. Boron Hugoniot data from impedance matching (IM) with a diamond standard. Shock velocities (U_s) at the IM interface were measured *in situ* using VISAR for quartz (Q) and inferred using the nonsteady waves correction [101–103] for boron (B) and diamond (C). U_s^C and U_s^B were used in the IM analysis to determine the particle velocity (u_p), pressure (P), and density (ρ) on the boron Hugoniot.

| U_s^Q | U_s^C | U_s^B | u_p^B | P^B | ρ^B |
|------------------|------------------|------------------|------------------|----------------|----------------------|
| (km/s) | (km/s) | (km/s) | (km/s) | (GPa) | (g/cm ³) |
| 55.18 ± 0.25 | 55.25 ± 0.74 | 58.71 ± 0.66 | 41.35 ± 0.82 | 5608 ± 118 | 7.811 ± 0.465 |

208 sample [101–103]. The Hugoniot and release for the diamond standard were calculated
 209 using a tabular equation of state (LEOS 9061 [104]) created from a multiphase model based
 210 on DFT-MD and PIMC calculations [105]. The experimental Hugoniot data are given in
 211 Table I.

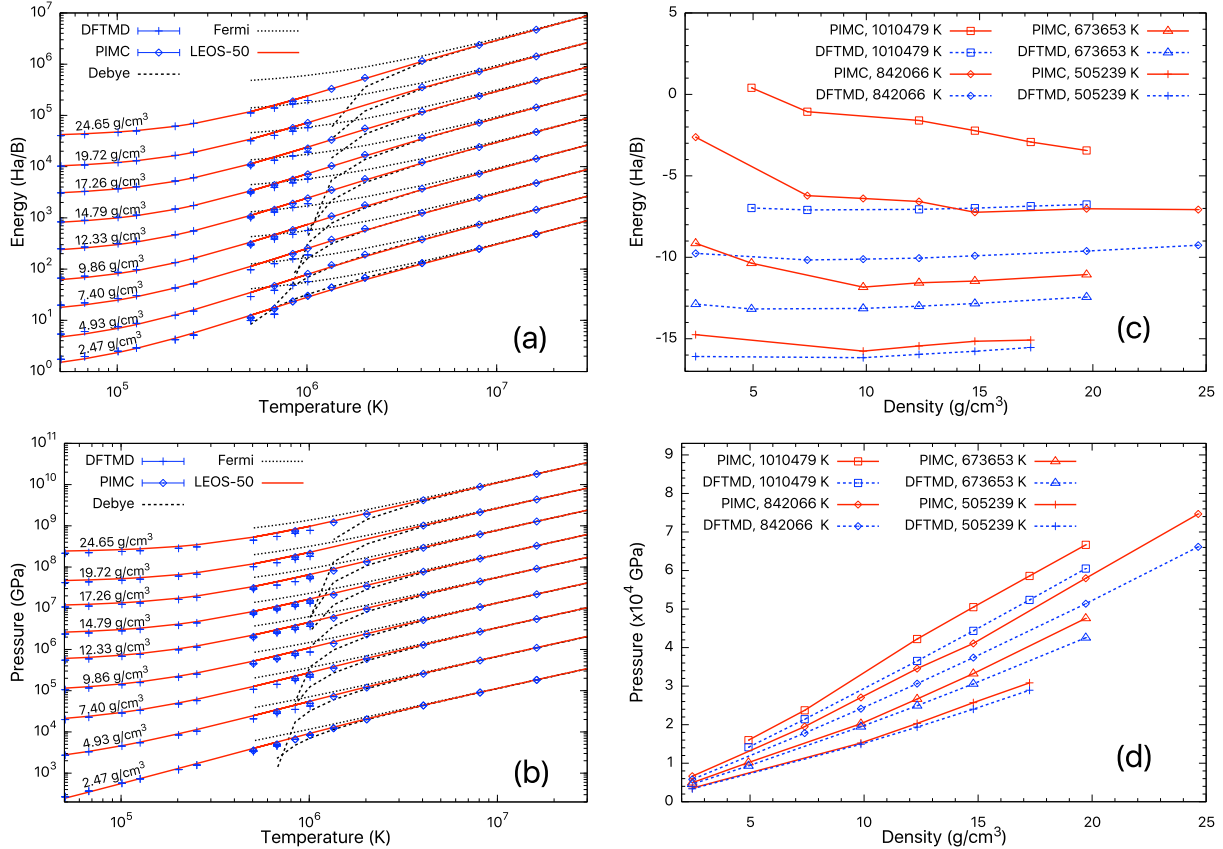


FIG. 3. (a) Energy- and (b) pressure-temperature EOS plots along isochores for boron from our PIMC and DFT-MD simulations. For comparison, the ideal Fermi-gas theory, Debye-Hückel model, and LEOS 50 are also shown. In (a), the LEOS 50 data have been aligned with DFT by setting their energies to be equal at 2.46 g/cm^3 and 0 K . Subplots (c) and (d) are the comparison in internal energy and pressure between PIMC and DFT-MD along four isotherms as functions of density. In subplots (a) and (b), results at different isochores have been shifted apart for clarity.

212 III. RESULTS

213 A. Equation of state

214 The first-principles EOS [106] computed with PIMC and DFT-MD calculations are shown
 215 in Figs. 3a and b. The internal energies and pressures we computed using PIMC are consis-
 216 tent with those predicted by the ideal Fermi gas theory and the Debye-Hückel model in the
 217 high temperature limit ($>1.6 \times 10^7 \text{ K}$) where these models are valid. At lower temperatures,
 218 ideal Fermi gas theory and Debye-Hückel model predictions become increasingly higher and

219 lower, respectively, than our PIMC values for both internal energy and pressure. This is
220 easily understood due to the increased contribution from electron-electron and electron-ion
221 correlations at lower temperature which render the high-temperature theories inadequate.
222 The PIMC energies and pressures show the same trend as those from our DFT-MD simula-
223 tions along all the nine isochores between ρ_0 – $10\rho_0$.

224 The explicit inclusion of electronic shell structures leads to significant differences in the
225 EOS of boron relative to the TF model, in particular at $T \leq 2 \times 10^6$ K. In comparison with
226 our first-principles data, the LEOS 50 pressures differ by a variation -16.4% to 7.1%, and
227 the internal energy differences are between -2.0–8.2 Ha/atom, at $T \leq 2.0 \times 10^6$ K. These
228 differences lead to significantly different peak compression in the shock Hugoniot curves, as
229 will be discussed in Sec. III B. At high temperatures ($T > 2 \times 10^6$ K), the relative differences
230 in energies and pressures are small (between -3.1% and 0.5% in pressure, and between -1%
231 and 6% in internal energy).

232 With decreasing temperature from 10^6 to 5.05×10^5 K, we find improved agreement be-
233 tween PIMC and DFT-MD results in both internal energy and pressure (Fig. 3c,d). We
234 define a critical temperature of 5.05×10^5 K corresponding to the temperature above which
235 significant ionization of the boron $1s^2$ core state is expected to render the pseudopotential
236 calculation inaccurate. This critical temperature is lower than what we found recently for
237 carbon in CH (10^6 – 2×10^6 K). This is due to the shallower $1s$ level in boron than in carbon.
238 At the critical temperature, we find good consistency between PIMC and DFT-MD, with
239 differences less than 1.5 Ha/B in energy and less than 5% in pressure.

240 The larger underestimation in energy and pressure by DFT-MD at higher densities and
241 temperatures can be attributed to the failure of the pseudopotential approximation at these
242 conditions. The significant compression at densities higher than $5\rho_0$ leads to the overlap of
243 the nearby frozen cores, which makes the use of the pseudopotential inaccurate at these con-
244 ditions. In previous studies, other authors have overcome the failure of the pseudopotential
245 by constructing all-electron pseudopotentials that maintain accuracy up to higher temper-
246 atures and densities [15, 107]. We note that the DFT-MD and PIMC EOS data reported
247 here are in good agreement with the all-electron pseudopotential results [108].

248 **B. Shock compression**

249 During planar shock compression, the locus of the final (shocked) state (E, P, V) is related
 250 to the initial (pre-shocked) state (E_0, P_0, V_0) via the Rankine-Hugoniot equation [109]

$$(E - E_0) + \frac{1}{2}(P + P_0)(V - V_0) = 0, \quad (1)$$

251 where E , P , and V denotes internal energy, pressure, and volume, respectively. Equation 1
 252 allows for determining the P - V - T Hugoniot conditions with the EOS data in Sec. III A.
 253 We determine the initial energy E_0 and pressure P_0 by performing DFT-MD simulations
 254 at 300 K for α -boron with an initial density $\rho_0 = 2.46 \text{ g/cm}^3$ throughout the manuscript,
 255 except when comparing with our experimental measurement for which E_0 and P_0 of β -boron
 256 with $\rho_0 = 2.31 \text{ g/cm}^3$ (same as that of the sample used in the experiment) are used.

257 We plot the Hugoniot curves thus obtained in a pressure-compression ratio $P - \rho/\rho_0$ and
 258 a temperature-pressure $T - P$ diagram in Fig. 4, and in a $T - \rho$ diagram in Fig. 1. Our
 259 EOS based on PIMC calculations predict a maximum compression of 4.6 at 0.85 gigabar
 260 pressure and 2.0 million K temperature. In comparison, ACTEX calculations [110] predict
 261 boron to behave similarly while LEOS 50 and SESAME 2330 models predict it to be stiffer
 262 by 6.9% and 5.5%, respectively, at the maximum compression. The difference originates
 263 from the 1s shell ionization, which increases the compression ratio and is well captured
 264 in the PIMC simulations but not in the TF-based LEOS 50 and SESAME 2330 models.
 265 A similar deviation has been found for other low-Z systems, such as CH [45, 46]. At lower
 266 temperatures, LEOS 50 predictions of the $P - \rho/\rho_0$ relation agree with our DFT-MD findings,
 267 while SESAME 2330 predicts boron to be softer by 6-10%. These are related to the specific
 268 details in constructing the cold curve and the thermal ionic parts in the EOS models.

269 The $T - P$ Hugoniot curves predicted by the different methods are very similar. In
 270 comparison with our PIMC/DFT-MD predictions in the 10^5 - 10^6 K regime, Thomas-Fermi
 271 based LEOS 50 and SESAME 2330 slightly underestimate the temperature for fixed pressure,
 272 while ACTEX temperatures are higher. We suspect this is related to the K shell occupations
 273 in the different theories and will put more detailed comparisons and discussions in a future
 274 publication.

275 The experimental boron Hugoniot data are summarized in Table I and compared with
 276 our theoretical predictions in a pressure-compression ratio plot (Fig. 5). The measured

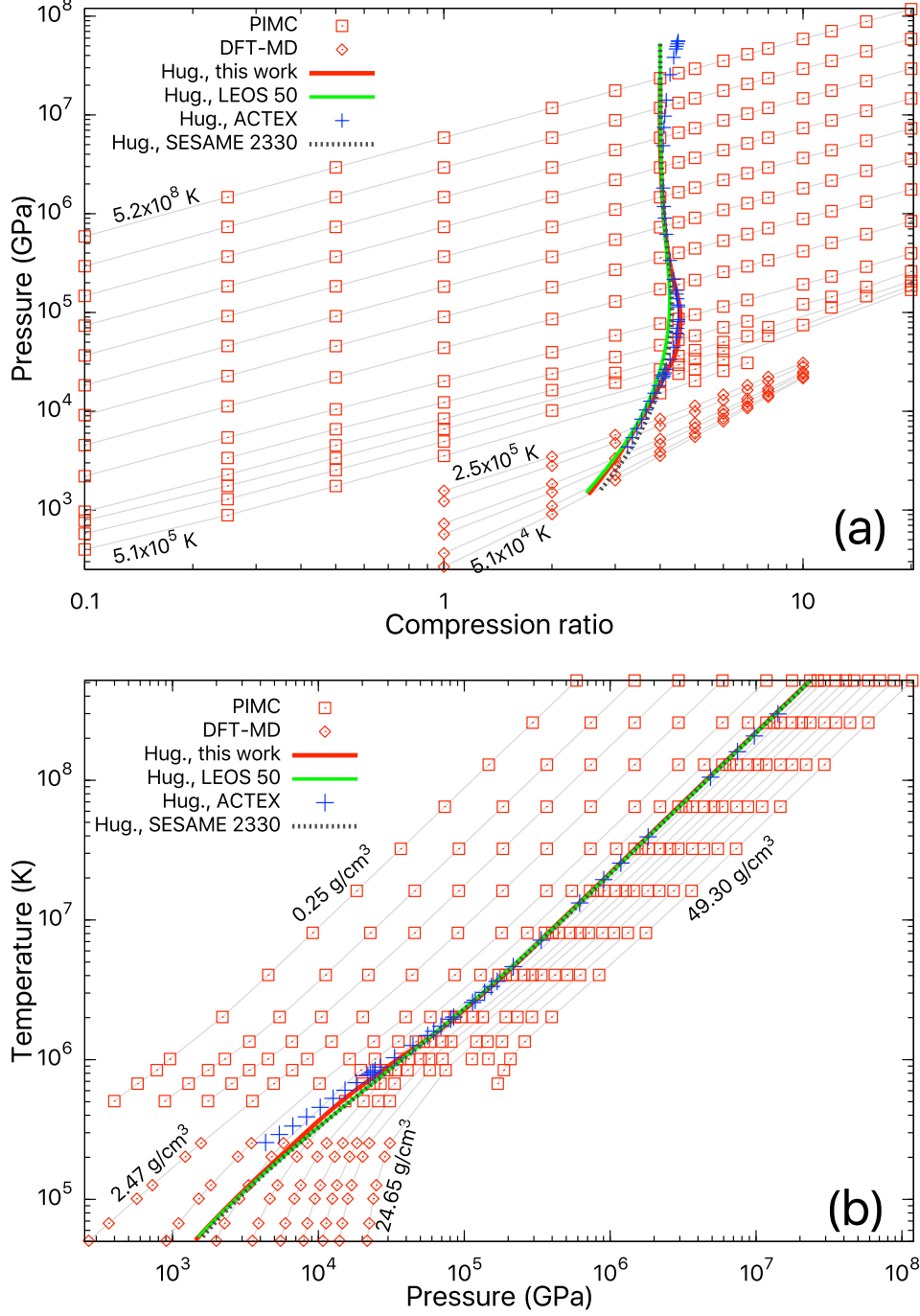


FIG. 4. Boron EOS and shock Hugoniot curves shown in (a) $P - \rho/\rho_0$ and (b) $T - P$ plots. The Hugoniot results from LEOS 50, [ACTEX](#), and SESAME 2330 are co-plotted for comparison. Gray-colored curves in panels (a) and (b) denote isotherms and isochores, respectively. The Hugoniot curves are constructed by choosing the initial density to be the same as ρ_0 (~ 2.46 g/cm³). The difference between ACTEX and others in (a) at $P > 10^7$ GPa is because of the inclusion of electronic relativistic effects in ACTEX.

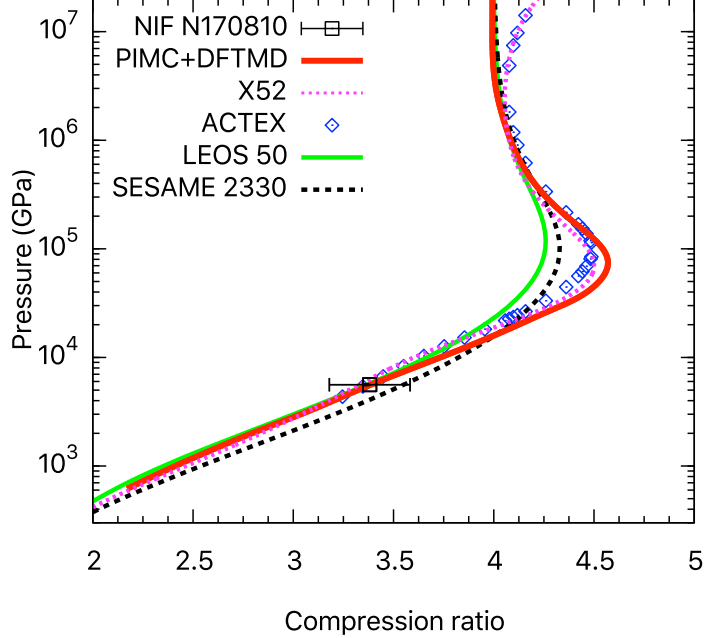


FIG. 5. Comparison of the experimental boron shock Hugoniot result with predictions from our first-principles EOS data and LEOS 50, SESAME 2330, X52 models and ACTEX. The initial density for the PIMC/DFT-MD, LEOS 50, SESAME 2330, and X52 curves are 2.31 g/cm^3 , i.e., the same as that of the experimental sample. The initial density for the ACTEX curve is 2.46 g/cm^3 .

277 data point agrees perfectly with predictions by our first-principles calculations, X52 [111],
 278 ACTEX, and LEOS 50, but the prediction from the SESAME 2330 model is also consistent
 279 with the measurement if the 1σ error bar in density is taken into account. The Hugoniot
 280 profiles by ACTEX and X52 are in excellent agreement with our PIMC and DFT-MD
 281 predictions. The minor mismatch in compression at 50-2000 Mbar is associated with the
 282 1-2% uncertainty in our PIMC/DFTMD Hugoniot curve because of the sparse data grid and
 283 non-smooth numerical EOS data.

284 IV. DISCUSSION

285 A. Static and dynamic properties of boron plasmas

286 The EOS and shock compression of warm and hot dense matter can be understood from
 287 the atomic and electronic structures. Figure 6 compares the ionic radial distribution function

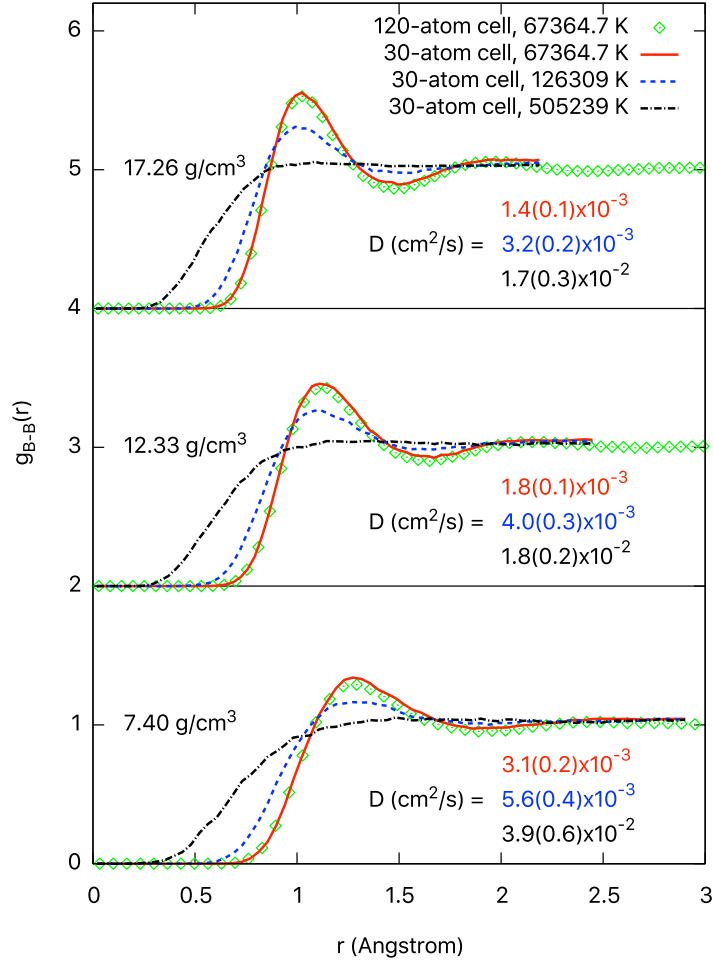


FIG. 6. Nuclear pair correlation function $g(r)$ of boron at three densities and three temperatures. The $g(r)$ curves analyzed based on MD simulations of 120-atom cells at 6736.47 K are co-plotted for comparison. Curves at different densities have been off set for clarity. The consistency between $g(r)$ of 30- and 120-atom cells show negligible finite size effect in describing the ionic structures. The numbers at the inset of each panel show the values of self diffusivity at the corresponding density. Numbers in parentheses denote the standard error of the corresponding data. Red, blue, and dark-colored texts correspond to temperatures of 6.7×10^4 , 1.3×10^5 , and 5.1×10^5 K, respectively.

288 $g(r)$ for boron at selected densities (3-, 5-, and 7-times ρ_0) and temperatures (6.74×10^4 ,
 289 1.26×10^5 , and 5.05×10^5 K) from our DFT-MD simulations. At 6.74×10^4 K, the $g(r)$ function
 290 shows a peak-valley feature between distances of 1.0–2.0 Å from the nucleus, which is
 291 characteristic of a bonding liquid. This feature gradually vanishes as temperature increases,
 292 indicating that the warm dense system being studied increasingly approaches an ideal gas,

293 in spite of the significant coupling effect that exists (Fig. 1) and the fact that the atoms are
 294 not charge-neutral but partially ionized, as we will discuss below.

295 The pressure-driven and thermal ionization processes can be well described by comparing
 296 the $N(r)$ functions, which denote the average number of electrons within distance r from
 297 each nucleus, with the corresponding profile of the B^{3+} ionization state. $N(r)$ curves that
 298 are fully above the profile for B^{3+} are associated with fully occupied K shells, while those
 299 falling below indicate K -shell ionization. The results at $0.1\times$, $1.0\times$, $4.0\times$, and $20\times\rho_0$ from
 300 our PIMC calculations are shown in Fig. 7. We find no observable ionization of the 1s
 301 states for $T < 0.5 \times 10^6$ K at $\rho > \rho_0$, which validates the use of the pseudopotential with a
 302 helium core in our DFT-MD simulations in these temperature and density conditions. As T
 303 exceeds 0.5×10^6 K, 1s electrons are excited and thus contribute to the total pressure and
 304 energy of the system, which explains why both quantities are underestimated in DFT-MD,
 305 as has been shown in Fig. 3 and discussed in Sec. III A.

306 The $N(r)$ results also show that it requires higher temperatures for the K shell to reach
 307 the same degree of ionization at higher densities and that the same temperature change is
 308 associated with larger degrees of K shell ionization at lower densities. Previous generalized
 309 chemical models [63] showed increasing fraction of B^{2+} particles at $T > 3.5 \times 10^4$ K and
 310 negligible K shell ionization within the complete temperature range (up to 4.2×10^4 K) of
 311 their study for low-density (0.094 g/cm^3) boron plasmas, which remarkably agree with our
 312 findings here based on first-principles calculations.

313 In order to elucidate the physical origin of these observations, we compare the temper-
 314 ature dependence of the 1s binding energy E_b^{1s} with the chemical potential E_{CP} along four
 315 different isochores between $0.1\times$ and $20\times\rho_0$. The results are obtained using the Purgatorio
 316 method [113] and are summarized in Fig. 8. As density increases, E_b^{1s} rises closer to the
 317 continuum level ($E=0$). E_{CP} also increases with increasing density, and in fact increases
 318 faster than E_b^{1s} . As a result, the Fermi occupation number of the 1s state actually increases
 319 with increasing density. At the temperature at which the E_b^{1s} and E_{CP} curves intersect, the
 320 1s energy level has a Fermi occupation number of $1/2$. The dash-dotted curves in Fig. 8 plot
 321 the chemical potential minus $5k_B T$. The 1s level will have a Fermi occupation number of
 322 just 0.67% below full occupancy at the temperature at which these curves intersect the cor-
 323 responding 1s energy levels. This intersection therefore indicates the critical temperature at
 324 which the 1s level starts to ionize. This intersection point shifts to higher temperature with

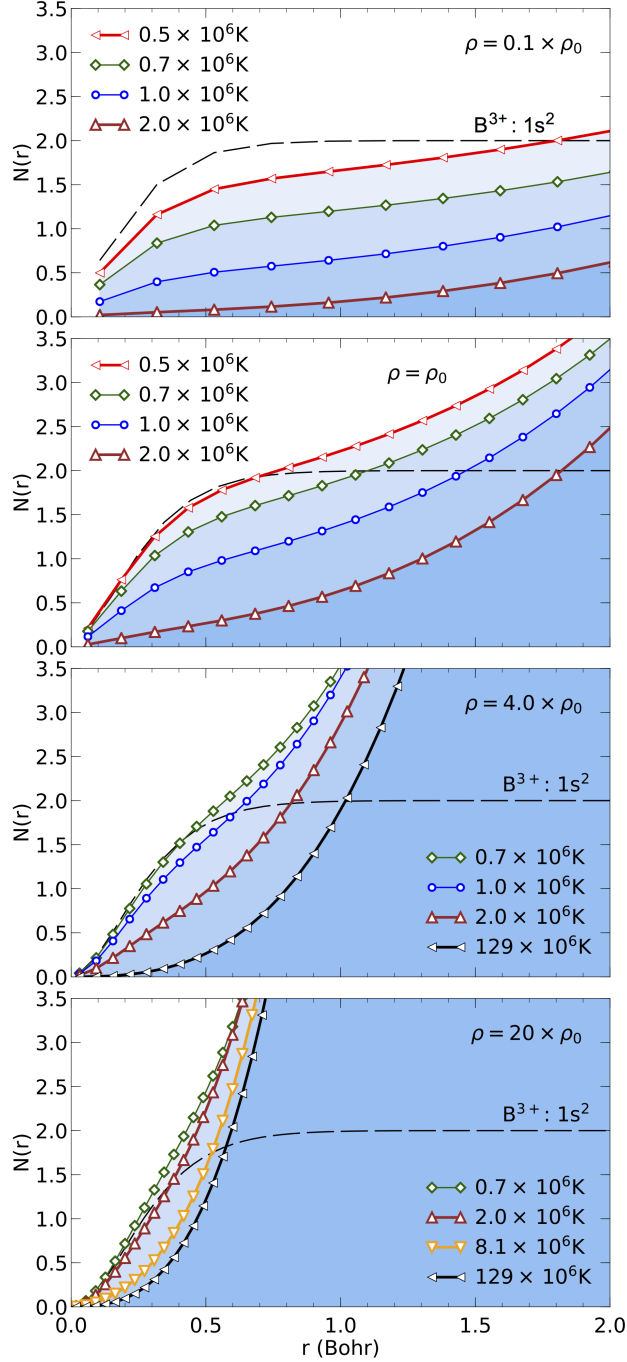


FIG. 7. The average number of electrons around each nucleus at different densities and a series of temperatures. $\rho_0 \approx 2.46 \text{ g/cm}^3$. The long dashed curve denotes the corresponding profile of the isolated B^{3+} ion. The profile was derived by integrating the doubly-occupied $1s$ orbitals that we computed with the GAMESS quantum chemistry code [112].

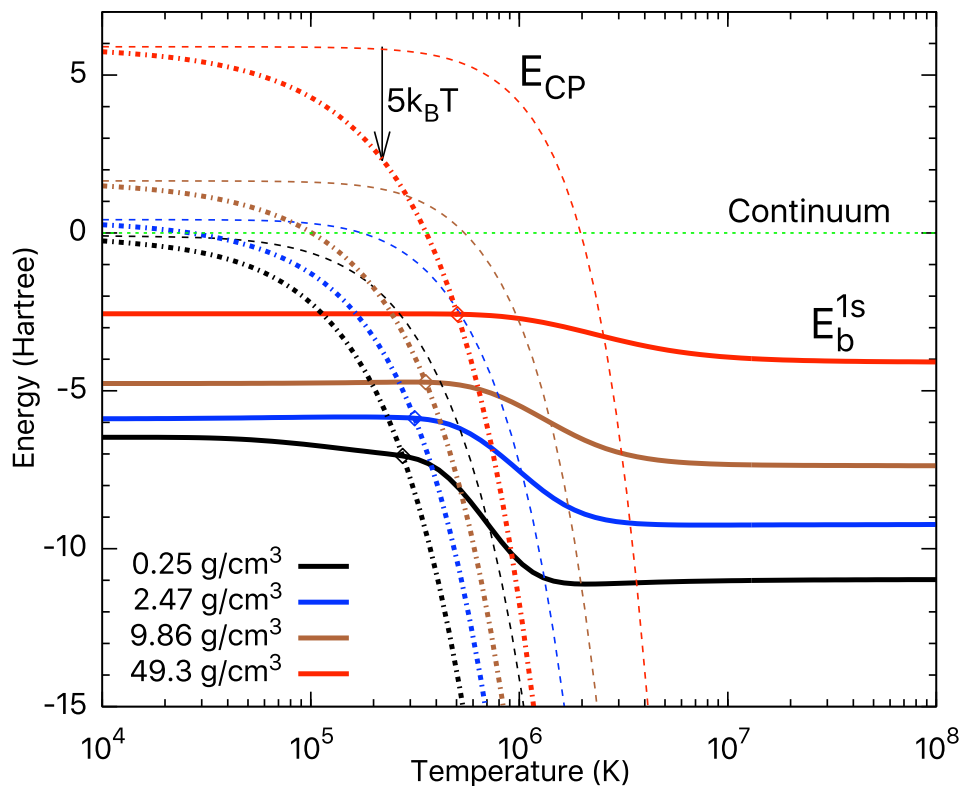


FIG. 8. Comparison of the 1s binding energy E_b^{1s} (solid curves) with the chemical potential E_{CP} (thin dashed curves) as functions of temperature at four densities. The data are obtained using the Purgatorio method. The dash-dotted curves represent $E_{CP} - 5k_B T$. The diamonds indicate the points at which the 1s level starts to be ionized (by 0.67%).

325 increasing density, indicating that the ionization temperature increases with density, even
 326 though the 1s binding energy itself decreases. This accounts for the higher temperatures
 327 that are required for the K shell to reach the same degree of ionization at higher densities,
 328 as observed in Fig. 7. Purgatorio calculations of the K -shell occupation refines the critical
 329 temperature to $3.2 \times 10^5 - 3.6 \times 10^5$ K at densities between $\rho_0 - 4\rho_0$. We have also compared the
 330 Purgatorio results to that of DFT simulations of boron on a face-centered cubic lattice using
 331 a dual-projector Optimized Norm-Conserving Vanderbilt (ONCV) [114, 115] pseudopotential
 332 with core radius equaling 0.8 Bohr. The ONCV and the Purgatorio results on chemical
 333 potential, K shell ionization energies, and K shell occupation are in good agreement with
 334 each other.

335 The above findings about ionization are also consistent with the upshifting in energy,

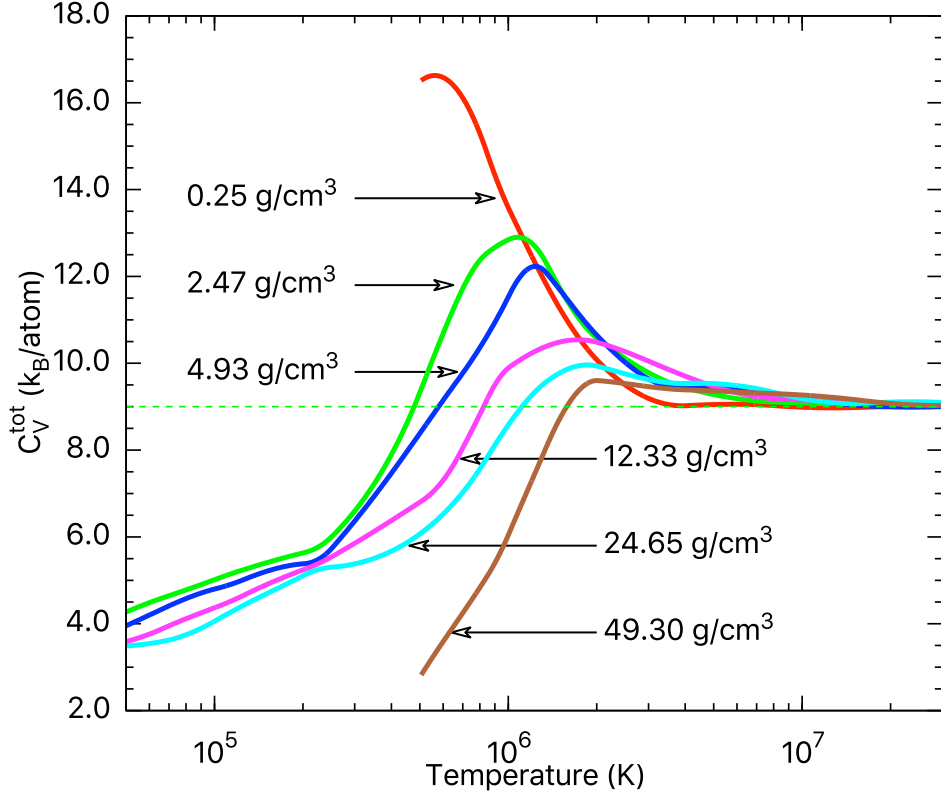


FIG. 9. Total heat capacity $C_V^{\text{tot}} = (\partial E / \partial T)|_V$ of boron obtained from our DFT-MD and PIMC data along several isochores. All curves converge to the ideal-gas limit of $9k_B/\text{atom}$ at high temperature.

336 decreasing in magnitude, and expanding in width of the peak in heat capacity (Fig. 9) as
 337 density increases. The peaks originate from the excitation of 1s electrons of boron and
 338 appear at lower temperatures than that of carbon in CH with comparable densities [46].
 339 This is because the K shell of boron is shallower than that of carbon.

340 We also estimate the self diffusion coefficient D for boron using $D = \text{MSD}/6t$, where the
 341 MSD denotes the mean square displacement and t is the simulation time [116]. We obtained
 342 values of D that range between 8×10^{-4} and $0.05 \text{ cm}^2/\text{s}$ at the temperatures (5×10^4 – 5×10^5
 343 K) and densities (ρ_0 – $10\rho_0$) that we performed DFT-MD simulations. We find the values of
 344 D (some shown in Fig. 6) monotonically increase with temperature and the specific volume.
 345 This is similar to what have been found for the diffusion of hydrogen in asymmetric binary
 346 ionic mixtures [117] and deuterium-tritium mixtures [118].

347 We note that accurate DFT-MD simulations of transport properties, such as diffusivity

TABLE II. Polar direct-drive exploding pushers performance sensitivity to pressure change in boron EOS. We consider the LEOS 50 model, with pressure multipliers (p_{mult}) listed in parentheses, as well as the new X52 model. Corresponding data based on a GDP model are also shown for comparison.

| EOS Model (p_{mult}) | Neutron Yield | Xray Bang Time (ns) | Gas Areal Density (mg/cm ²) | Shell Areal Density (mg/cm ²) | Convergence Ratio | Burn-averaged Ion Temperature (keV) |
|--------------------------|-----------------------|---------------------|---|---|-------------------|-------------------------------------|
| LEOS 50 (0.8) | 2.15×10^{13} | 2.10 | 3.53 | 2.75 | 3.80 | 16.2 |
| LEOS 50 (1.0) | 3.60×10^{13} | 2.13 | 4.99 | 3.27 | 4.53 | 17.2 |
| LEOS 50 (1.2) | 5.70×10^{13} | 2.18 | 7.38 | 4.12 | 5.60 | 17.5 |
| X52 (1.0) | 3.53×10^{13} | 2.13 | 4.91 | 3.25 | 4.50 | 17.2 |
| GDP model from Ref. 2 | 2.14×10^{13} | 3.17 | 17.5 | 29.1 | 12.29 | 7.80 |

and viscosity, of one component plasmas across a wide coupling regime are useful because of the potential breakdown of laws for ordinary condensed matter (e.g., the Arrhenius relation) [119]. These studies also build the base for estimating the corresponding properties of mixtures [118] which, together with EOS approximations (e.g., average-atom or linear mixing approximation [45, 46]), are important in characterizing multi-component plasmas. However, such simulations require much more extended length of the MD trajectories and range of temperatures and densities in the more strongly-coupled regime, which are beyond the scope of this work.

B. PDXP performance sensitivity to EOS

In Ref. 2, a 1D Ares [120, 121] model for the PDXP platform with GDP capsules was developed to match the x-ray bang time and yield of N160920-003, N160920-005, and N160921-001. While we anticipate that changing the ablator in these experiments would necessitate recalibration of this model to match the performance of a new material, this model nonetheless offers a reasonable starting point for examining EOS sensitivity. The capsule in N160920-005 consisted of a 18 μm thick GDP shell with an outer diameter of 2.95 mm, filled with 8-bar of D₂ gas and a trace amount of argon as a spectroscopic tracer. The implosion was driven by a 1.8 ns square pulse corresponding to a peak intensity of about 9.7×10^{14} W/cm². The model developed in Ref. 2 incorporates a multiplier on the energy delivered to the capsule, a flux limiter on the electron thermal conduction to account for inadequacies in the assumption of the diffusion model for heat transport, and a multiplier on the mass diffusion coefficient that is used to calibrate the multi-component Navier-Stokes model for mixing of the capsule ablator into the deuterium fuel. The authors also modify the laser intensity

370 used in the 1D simulations to account for geometric losses based on 2D Ares simulations. As
 371 discussed in Sec. III A, our *ab initio* simulations yield pressures that differ by up to 20% from
 372 the existing LEOS 50 table. The largest variations occur at temperatures between about
 373 1×10^5 and 5×10^6 K, as shown in Fig. 3. In this regime, the electron thermal pressure is the
 374 largest contribution to the total pressure. We initially performed 1D Ares simulations using
 375 the LEOS 50 table with pressure multipliers of 0.8, 1.0, and 1.2 as a means of estimating
 376 the EOS sensitivity in a PDXP capsule using a boron ablator. We subsequently extended
 377 this sensitivity study to include the X52 model, which is based on Purgatorio and has been
 378 semi-empirically fit to agree with the PIMC, DFT, and ACTEX isochores.

379 Because boron is substantially more dense than GDP (2.46 g/cm^3 compared to 1.05
 380 g/cm^3), and because the higher tensile strength should allow for a thinner shell, we have
 381 chosen a thickness of $6 \text{ }\mu\text{m}$ for the boron capsules. The use of a thinner ablator may
 382 reduce the effects of presumed mix in the capsules relative to the model calibrated for GDP.
 383 We therefore performed simulations of the boron PDXP model without the diffusive mix
 384 model, instead assuming a fall line model to estimate the impact of mix on the yield. The
 385 results of the EOS sensitivity study are shown in Table II. We find that applying pressure
 386 multipliers to LEOS 50 results in yield variations of -40% to +58%. Higher ablator pressures
 387 result in higher gas areal density and higher convergence at burn time for very similar ion
 388 temperatures, thus the impact on yield is generated primarily via higher compression of
 389 the D_2 gas as the pressure in the ablator increases. The shell areal density at the time of
 390 peak neutron production is also impacted by the pressure multiplier. In contrast, the new
 391 X52 model for boron gives results that are much more similar to LEOS 50, substantially
 392 narrowing the range of EOS-dependent uncertainty in the capsule yield.

393 The reason for the good agreement in capsule performance for LEOS 50 and X52 is
 394 that the pressure differences that were observed between the *ab initio* simulations and the
 395 LEOS 50 table are concomitant with differences in the internal energy, and the X52 model
 396 accounts for changes to both of these quantities. This demonstrates the importance of
 397 constraining both the pressure and the internal energy in EOS models that are used for
 398 radiation-hydrodynamic simulations.

399 For reference, the results from the model calculations in Ref. 2 are also listed in Table II.
 400 We find that the 1D Ares model predicts lower gas and much lower shell areal density at
 401 peak burn time for the boron ablator compared to GDP. This is because a larger portion of

402 the thinner boron shell is ablated, allowing behavior more like a true exploding pusher than
403 the thicker GDP ablator. The GDP design has a substantial amount of unablated plastic,
404 leading to a lower implosion velocity, higher convergence, and lower ion temperatures relative
405 to the boron ablator.

406 V. CONCLUSIONS

407 In this work, we present first-principles EOS results of boron using PIMC and DFT-
408 MD simulations from temperatures of 5×10^4 K to 5.2×10^8 K. PIMC and DFT-MD cross-
409 validates each other by showing remarkable consistency in the EOS (<1.5 Ha/B in total
410 internal energy and $<5\%$ in total pressure) at 5×10^5 K. Our [high-accuracy](#) EOS for boron
411 provides an important base for future theoretical investigations of plasmas with boron.

412 We measured the boron Hugoniot at the highest pressure to date (56.1 ± 1.2 Mbar) in a
413 dynamic compression experiment at NIF. [The result shows excellent agreement with that ob-](#)
414 [tained from our first-principles EOS data based on DFT-MD calculations.](#) The experimental
415 data point also agrees well with predictions by a TF model LEOS 50, the Purgatorio-based
416 X52, and ACTEX calculations, and is consistent with those by the TF-based SESAME 2330
417 if considering the 1σ error bar in density. In addition, our PIMC calculations predict a max-
418 imum compression of 4.6, which originates from K shell ionization and is slightly larger than
419 those predicted by TF models LEOS 50 and SESAME 2330. It requires more, high-precision
420 experiments to test these predictions in these high pressures, temperature regimes.

421 We investigated the PDXP performance sensitivity to the EOS with a 1D hydrodynamic
422 model. The simulation results show that variations in pressure by -20% and 20% result in
423 neutron yield variations of -40% to $+58\%$, respectively. In contrast, the new X52 model
424 for boron gives results that are much more similar to LEOS 50, substantially narrowing the
425 range of EOS-dependent uncertainty in the capsule yield. This demonstrates the importance
426 of constraining both the pressure and the internal energy in EOS models that are used for
427 radiation-hydrodynamic simulations.

428 **ACKNOWLEDGMENTS**

429 We thank C. Leland Ellison for providing support in running the 1D Ares model for
430 the boron capsules. This research is supported by the U. S. Department of Energy, grant
431 DE-SC0016248. Computational support was mainly provided by the Blue Waters sustained-
432 petascale computing project (NSF ACI 1640776), which is supported by the National Science
433 Foundation (awards OCI-0725070 and ACI-1238993) and the state of Illinois. Blue Waters
434 is a joint effort of the University of Illinois at Urbana-Champaign and its National Center for
435 Supercomputing Applications. S.Z. is partially supported by the PLS-Postdoctoral Grant
436 of the Lawrence Livermore National Laboratory. S.Z. appreciates Dr. Babak Sadigh for
437 helpful discussion about thermostat. This work was in part performed under the auspices of
438 the U.S. Department of Energy by Lawrence Livermore National Laboratory under Contract
439 No. DE-AC52-07NA27344.

-
- 440 [1] M. G. Johnson, D. T. Casey, M. Hohenberger, A. B. Zylstra, A. Bacher, C. R. Brune, R. M.
441 Bionta, R. S. Craxton, C. L. Ellison, M. Farrell, J. A. Frenje, W. Garbett, E. M. Garcia, G. P.
442 Grim, E. Hartouni, R. Hatarik, H. W. Herrmann, M. Hohensee, D. M. Holunga, M. Hoppe,
443 M. Jackson, N. Kabadi, S. F. Khan, J. D. Kilkenny, T. R. Kohut, B. Lahmann, H. P. Le,
444 C. K. Li, L. Masse, P. W. McKenty, D. P. McNabb, A. Nikroo, T. G. Parham, C. E. Parker,
445 R. D. Petrasso, J. Pino, B. Remington, N. G. Rice, H. G. Rinderknecht, M. J. Rosenberg,
446 J. Sanchez, D. B. Sayre, M. E. Schoff, C. M. Shulldberg, F. H. Sguin, H. Sio, Z. B. Walters,
447 and H. D. Whitley, *Phys. Plasmas* **25**, 056303 (2018).
- 448 [2] C. L. Ellison, H. D. Whitley, C. R. D. Brown, S. R. Copeland, W. Garbett, H. Le, M. B.
449 Schneider, Z. B. Walters, H. Chen, J. I. Castor, R. S. Craxton, M. Gatu Johnson, E. M.
450 Garcia, F. R. Graziani, J. C. Hayes, G. E. Kemp, C. M. Krauland, P. W. McKenty, B.
451 Lahmann, J. E. Pino, M. S. Rubery, H. A. Scott, and R. Shepherd, accepted to be published
452 in *Phys. Plasmas*..
- 453 [3] Probing the Physics of Burning DT Capsules Using Gamma-ray Diagnostics, A.
454 C. Hayes-Sterbenz, G. M. Hale, G. Jungman, and M. W. Park, LA-UR-15-20627,
455 <http://permalink.lanl.gov/object/tr?what=info:lanl-repo/lareport/LA-UR-15-20627>.

- 456 [4] B. Hammel, S. Haan, D. Clark, M. Edwards, S. Langer, M. Marinak, M. Patel, J. Salmonson,
457 and H. Scott, High Energ. Dens. Phys. **6**, 171 (2010).
- 458 [5] H. F. Robey, J. D. Moody, P. M. Celliers, J. S. Ross, J. Ralph, S. Le Pape, L. Berzak Hopkins,
459 T. Parham, J. Sater, E. R. Mapoles, D. M. Holunga, C. F. Walters, B. J. Haid, B. J.
460 Koziowski, R. J. Dylla-Spears, K. G. Krauter, G. Frieders, G. Ross, M. W. Bowers,
461 D. J. Strozzi, B. E. Yoxall, A. V. Hamza, B. Dzenitis, S. D. Bhandarkar, B. Young, B. M.
462 Van Woutherghem, L. J. Atherton, O. L. Landen, M. J. Edwards, and T. R. Boehly, Phys.
463 Rev. Lett. **111**, 065003 (2013).
- 464 [6] V. A. Smalyuk, D. T. Casey, D. S. Clark, M. J. Edwards, S. W. Haan, A. Hamza, D. E.
465 Hoover, W. W. Hsing, O. Hurricane, J. D. Kilkenny, J. Kroll, O. L. Landen, A. Moore,
466 A. Nikroo, L. Peterson, K. Raman, B. A. Remington, H. F. Robey, S. V. Weber, and
467 K. Widmann, Phys. Rev. Lett. **112**, 185003 (2014).
- 468 [7] S. X. Hu, V. N. Goncharov, T. R. Boehly, R. L. McCrory, S. Skupsky, L. A. Collins, J. D.
469 Kress, and B. Militzer, Phys. Plasmas **22**, 056304 (2015).
- 470 [8] S. X. Hu, L. A. Collins, V. N. Goncharov, J. D. Kress, R. L. McCrory, and S. Skupsky,
471 Phys. Rev. E **92**, 043104 (2015).
- 472 [9] R. M. More, K. H. Warren, D. A. Young, and G. B. Zimmerman, Phys. Fluids **31**, 3059
473 (1988).
- 474 [10] D. A. Young and E. M. Corey, J. Appl. Phys. **78**, 3748 (1995).
- 475 [11] D. A. Liberman, Phys. Rev. B **20**, 4981 (1979).
- 476 [12] B. Wilson, V. Sonnad, P. Sterne, and W. Isaacs, J. Quant. Spectrosc. Radiat. Transfer **99**,
477 658 (2006).
- 478 [13] P. Sterne, S. Hansen, B. Wilson, and W. Isaacs, High Energ. Dens. Phys. **3**, 278 (2007).
- 479 [14] F. Lambert, J. Cl  rouin, and G. Z  erah, Phys. Rev. E **73**, 016403 (2006).
- 480 [15] J.-F. Danel, L. Kazandjian, and G. Zrah, Phys. Plasmas **19**, 122712 (2012).
- 481 [16] S. Zhang, H. Wang, W. Kang, P. Zhang, and X. T. He, Phys. Plasmas **23**, 042707 (2016).
- 482 [17] P. Hohenberg and W. Kohn, Phys. Rev. **136**, B864 (1964).
- 483 [18] W. Kohn and L. J. Sham, Phys. Rev. **140**, A1133 (1965).
- 484 [19] N. D. Mermin, Phys. Rev. **137**, A1441 (1965).
- 485 [20] F. J. Rogers, Astrophys. J. **310**, 723 (1986).
- 486 [21] F. J. Rogers, *Equation of State in Astrophysics*, IAU Colloquium 147, pp. 16-42, eds. G.

- 487 Chabrier & E. Schatzman (Cambridge Univ. Press, Cambridge, 1994).
- 488 [22] F. J. Rogers, F. J. Swenson, and C. A. Iglesias, *Astrophys. J.* **456**, 902 (1996).
- 489 [23] E. Pollock and D. Ceperley, *Phys. Rev. B* **30**, 2555 (1984).
- 490 [24] E. L. Pollock, *Comput. Phys. Commun.* **52**, 49 (1988).
- 491 [25] D. M. Ceperley, *Rev. Mod. Phys.* **67**, 279 (1995).
- 492 [26] D. M. Ceperley, in *Monte Carlo and Molecular Dynamics of Condensed Matter Systems*
493 (Editrice Compositori, Bologna, Italy, 1996) p. 443.
- 494 [27] B. Militzer and K. P. Driver, *Phys. Rev. Lett.* **115**, 176403 (2015).
- 495 [28] C. Pierleoni, M. A. Morales, G. Rillo, M. Holzmann, and D. M. Ceperley, *Proc. Natl. Acad.*
496 *Sci. USA* **113**, 4953 (2016).
- 497 [29] G. Mazzola, R. Helled, and S. Sorella, *Phys. Rev. Lett.* **120**, 025701 (2018).
- 498 [30] F. J. Rogers and H. E. DeWitt, *Phys. Rev. A* **8**, 1061 (1973).
- 499 [31] F. J. Rogers, *Phys. Rev. A* **10**, 2441 (1974).
- 500 [32] F. J. Rogers, *Phys. Rev. A* **19**, 375 (1979).
- 501 [33] F. J. Rogers, *Phys. Rev. A* **24**, 1531 (1981).
- 502 [34] F. J. Rogers and C. A. Iglesias, *Science* **263**, 50 (1994).
- 503 [35] F. J. Rogers and D. A. Young, *Phys. Rev. E* **56**, 5876 (1997).
- 504 [36] C. Pierleoni, D. M. Ceperley, B. Bernu, and W. R. Magro, *Phys. Rev. Lett.* **73**, 2145 (1994).
- 505 [37] K. P. Driver and B. Militzer, *Phys. Rev. Lett.* **108**, 115502 (2012).
- 506 [38] D. M. Ceperley, *J. Stat. Phys.* **63**, 1237 (1991).
- 507 [39] K. P. Driver and B. Militzer, *Phys. Rev. B* **93**, 064101 (2016).
- 508 [40] K. P. Driver, F. Soubiran, S. Zhang, and B. Militzer, *J. Chem. Phys.* **143**, 164507 (2015).
- 509 [41] K. P. Driver and B. Militzer, *Phys. Rev. B* **91**, 045103 (2015).
- 510 [42] S. Zhang, K. P. Driver, F. Soubiran, and B. Militzer, *High Energ. Dens. Phys.* **21**, 16 (2016).
- 511 [43] S. Zhang, K. P. Driver, F. Soubiran, and B. Militzer, *J. Chem. Phys.* **146**, 074505 (2017).
- 512 [44] K. P. Driver and B. Militzer, *Phys. Rev. E* **95**, 043205 (2017).
- 513 [45] S. Zhang, K. P. Driver, F. Soubiran, and B. Militzer, *Phys. Rev. E* **96**, 013204 (2017).
- 514 [46] S. Zhang, B. Militzer, L. X. Benedict, F. Soubiran, P. A. Sterne, and K. P. Driver, *J. Chem.*
515 *Phys.* **148**, 102318 (2018).
- 516 [47] A. Masago, K. Shirai, and H. Katayama-Yoshida, *Phys. Rev. B* **73**, 104102 (2006).
- 517 [48] S. Shang, Y. Wang, R. Arroyave, and Z.-K. Liu, *Phys. Rev. B* **75**, 092101 (2007).

- 518 [49] M. J. van Setten, M. A. Uijttewaal, G. A. de Wijs, and R. A. de Groot, *Journal of the*
519 *American Chemical Society* **129**, 2458 (2007).
- 520 [50] M. A. White, A. B. Cerqueira, C. A. Whitman, M. B. Johnson, and T. Ogitsu, *Angewandte*
521 *Chemie* **127**, 3697 (2015).
- 522 [51] T. Ogitsu, F. Gygi, J. Reed, Y. Motome, E. Schwegler, and G. Galli, *Journal of the American*
523 *Chemical Society* **131**, 1903 (2009).
- 524 [52] T. Ogitsu, E. Schwegler, and G. Galli, *Chem. Rev.* **113**, 3425 (2013).
- 525 [53] Y. Ma, C. T. Prewitt, G. Zou, H.-k. Mao, and R. J. Hemley, *Phys. Rev. B* **67**, 174116
526 (2003).
- 527 [54] E. Y. Zarechnaya, L. Dubrovinsky, N. Dubrovinskaia, Y. Filinchuk, D. Chernyshov,
528 V. Dmitriev, N. Miyajima, A. El Goresy, H. F. Braun, S. Van Smaalen, I. Kantor, A. Kantor,
529 V. Prakapenka, M. Hanfland, A. S. Mikhaylushkin, I. A. Abrikosov, and S. I. Simak, *Phys.*
530 *Rev. Lett.* **102**, 185501 (2009).
- 531 [55] G. Parakhonskiy, N. Dubrovinskaia, E. Bykova, R. Wirth, and L. Dubrovinsky, *Sci. Rep.* **1**,
532 96 (2011).
- 533 [56] O. O. Kurakevych, Y. L. Godec, T. Hammouda, and C. Goujon, *High Pressure Research*
534 **32**, 30 (2012).
- 535 [57] J. Qin, T. Irifune, H. Dekura, H. Ohfuji, N. Nishiyama, L. Lei, and T. Shinmei, *Phys. Rev.*
536 *B* **85**, 014107 (2012).
- 537 [58] V. L. Solozhenko and O. O. Kurakevych, **3**, 2351 (2013).
- 538 [59] A. R. Oganov, J. Chen, C. Gatti, Y. Ma, Y. Ma, C. W. Glass, Z. Liu, T. Yu, O. O. Ku-
539 rakevych, and V. L. Solozhenko, *Nature* **457**, 863 (2009).
- 540 [60] K. Shirai, *Jpn. J. Appl. Phys.* **56**, 05FA06 (2017).
- 541 [61] N. Vast, S. Bernard, and G. Zerah, *Phys. Rev. B* **52**, 4123 (1995).
- 542 [62] D. L. Price, A. Alatas, L. Hennet, N. Jakse, S. Krishnan, A. Pasturel, I. Pozdnyakova, M.-L.
543 Saboungi, A. Said, R. Scheunemann, W. Schirmacher, and H. Sinn, *Phys. Rev. B* **79**, 134201
544 (2009).
- 545 [63] E. M. Apfelbaum, *Contrib. Plasm. Phys.* **53**, 317 (2013).
- 546 [64] J. Cl erouin, P. Renaudin, and P. Noiret, *Phys. Rev. E* **77**, 026409 (2008).
- 547 [65] J. Cl erouin, P. Noiret, P. Blottiau, V. Recoules, B. Siberchicot, P. Renaudin, C. Blancard,
548 G. Faussurier, B. Holst, and C. E. Starrett, *Phys. Plasmas* **19**, 082702 (2012).

- 549 [66] J. Clérrouin, C. Starrett, G. Faussurier, C. Blancard, P. Noiret, and P. Renaudin, *Phys. Rev.*
550 *E* **82**, 046402 (2010).
- 551 [67] W. Johnson, C. Guet, and G. Bertsch, *J. Quant. Spectrosc. Radiat. Transfer* **99**, 327 (2006).
- 552 [68] G. Faussurier, C. Blancard, P. Coss, and P. Renaudin, *Phys. Plasmas* **17**, 052707 (2010).
- 553 [69] C. Blancard and G. Faussurier, *Phys. Rev. E* **69**, 016409 (2004).
- 554 [70] S. Kuhlbrodt, B. Holst, and R. Redmer, *Contrib. Plasm. Phys.* **45**, 73 (2005).
- 555 [71] LASL Shock Hugoniot Data, edited by S. P. Marsh (University of California Press, Berkeley,
556 1980).
- 557 [72] S. Le Pape, A. A. Correa, C. Fortmann, P. Neumayer, T. Döppner, P. Davis, T. Ma, L. Divol,
558 K.-U. Plagemann, E. Schwegler, R. Redmer, and S. Glenzer, *New J. Phys.* **15**, 085011 (2013).
- 559 [73] S. P. Lyon and J. D. Johnson, eds., *SESAME: The Los Alamos National Laboratory Equation*
560 *of State Database* (Group T-1, Report No. LA-UR-92-3407, 1992).
- 561 [74] B. Militzer, Ph.D. Thesis, University of Illinois at Urbana-Champaign (2000).
- 562 [75] W. R. Magro, D. M. Ceperley, C. Pierleoni, and B. Bernu, *Phys. Rev. Lett.* **76**, 1240 (1996).
- 563 [76] B. Militzer and D. M. Ceperley, *Phys. Rev. E* **63**, 066404 (2001).
- 564 [77] B. Militzer, D. M. Ceperley, J. D. Kress, J. D. Johnson, L. A. Collins, and S. Mazevet, *Phys.*
565 *Rev. Lett.* **87**, 275502 (2001).
- 566 [78] S. X. Hu, B. Militzer, V. N. Goncharov, and S. Skupsky, *Phys. Rev. Lett.* **104**, 235003
567 (2010).
- 568 [79] B. Militzer and D. M. Ceperley, *Phys. Rev. Lett.* **85**, 1890 (2000).
- 569 [80] S. X. Hu, B. Militzer, V. N. Goncharov, and S. Skupsky, *Phys. Rev. B* **84**, 224109 (2011).
- 570 [81] B. Militzer, W. Magro, and D. Ceperley, *Contrib. Plasm. Phys.* **39**, 151 (1999).
- 571 [82] B. Militzer and R. L. Graham, *J. Phys. Chem. Solids* **67**, 2136 (2006).
- 572 [83] B. Militzer, *Phys. Rev. Lett.* **97**, 175501 (2006).
- 573 [84] B. Militzer, *J. Low Temp. Phys.* **139**, 739 (2005).
- 574 [85] V. Natoli and D. M. Ceperley, *J. Comp. Phys.* **117**, 171 (1995).
- 575 [86] B. Militzer, *Comput. Phys. Commun.* **204**, 88 (2016).
- 576 [87] P. E. Blöchl, O. Jepsen, and O. K. Andersen, *Phys. Rev. B* **49**, 16223 (1994).
- 577 [88] G. Kresse and J. Furthmüller, *Phys. Rev. B* **54**, 11169 (1996).
- 578 [89] J. P. Perdew, K. Burke, and M. Ernzerhof, *Phys. Rev. Lett.* **77**, 3865 (1996).
- 579 [90] T. Ogitsu, F. m. c. Gygi, J. Reed, M. Udagawa, Y. Motome, E. Schwegler, and G. Galli,

- 580 Phys. Rev. B **81**, 020102 (2010).
- 581 [91] D. L. V. K. Prasad, M. M. Balakrishnarajan, and E. D. Jemmis, Phys. Rev. B **72**, 195102
582 (2005).
- 583 [92] B. Siberchicot, Phys. Rev. B **79**, 224101 (2009).
- 584 [93] S. Nosé, J. Chem. Phys. **81**, 511 (1984).
- 585 [94] See <http://opium.sourceforge.net> for information about the OPIUM code.
- 586 [95] G. Will and B. Kiefer, Zeitschrift für anorganische und allgemeine Chemie **627**, 2100 (2001).
- 587 [96] The radiation correction was added to our first-principles EOS by considering an ideal black
588 body scenario. Details about the way of adding this correction have been shown in our previ-
589 ous work (Ref. 43). In comparison with electronic relativistic effects, the radiation correction
590 becomes evident along the Hugoniot curve at a lower temperature; whereas in both cases the
591 compression ratio approaches the limit of 7 at high temperature.
- 592 [97] E. I. Moses, R. N. Boyd, B. A. Remington, C. J. Keane, and R. Al-Ayat, Phys. Plasmas **16**,
593 041006 (2009).
- 594 [98] L. V. Al'tshuler, K. K. Krupnikov, and M. I. Brazhnik, Sov. Phys. JETP **34**, 614 (1958).
- 595 [99] E. L. Dewald, K. M. Campbell, R. E. Turner, J. P. Holder, O. L. Landen, S. H. Glenzer, R. L.
596 Kauffman, L. J. Suter, M. Landon, M. Rhodes, and D. Lee, Review of Scientific Instruments
597 **75**, 3759 (2004).
- 598 [100] P. M. Celliers, D. K. Bradley, G. W. Collins, D. G. Hicks, T. R. Boehly, and W. J. Armstrong,
599 Rev. Sci. Instrum. **75**, 4916 (2004).
- 600 [101] D. E. Fratanduono, D. H. Munro, P. M. Celliers, and G. W. Collins, J. Appl. Phys. **116**,
601 033517 (2014).
- 602 [102] M. C. Gregor, D. E. Fratanduono, C. A. McCoy, D. N. Polsin, A. Sorce, J. R. Rygg, G. W.
603 Collins, T. Braun, P. M. Celliers, J. H. Eggert, D. D. Meyerhofer, and T. R. Boehly, Phys.
604 Rev. B **95**, 144114 (2017).
- 605 [103] D. E. Fratanduono, P. M. Celliers, D. G. Braun, P. A. Sterne, S. Hamel, A. Shamp, E. Zurek,
606 K. J. Wu, A. E. Lazicki, M. Millot, and G. W. Collins, Phys. Rev. B **94**, 184107 (2016).
- 607 [104] [We have tried re-analyzing our data using three different diamond EOS models, including
608 LEOS 64, LEOS 65, and SESAME 7834 and found the spread in the boron Hugoniot points
609 using the three diamond tables is within the error bar.](#)
- 610 [105] L. X. Benedict, K. P. Driver, S. Hamel, B. Militzer, T. Qi, A. A. Correa, A. Saul, and

611 E. Schwegler, Phys. Rev. B **89**, 224109 (2014).

612 [106] See Supplemental Material at [URL to be inserted by publisher] for the EOS data table of
613 boron from this study.

614 [107] S. Mazevet, F. Lambert, F. Bottin, G. Zérah, and J. Clérouin, Phys. Rev. E **75**, 056404
615 (2007).

616 [108] We perform DFT-MD simulations using our plane-wave pseudopotential code [122] and a self-
617 built all-electron ONCV [114, 115] pseudopotential at selected densities and temperatures
618 in the range of 8.71–87.08 eV. The ONCV pseudopotential has a small core radius of 0.8
619 Bohr. The simulations are based on 30-atom cells and the initial configurations are from
620 our VASP simulations at corresponding temperatures and densities. Our results show the
621 pressure between ONCV and VASP calculations generally agree very well at $T = 8.71$ eV.
622 We only find differences of up to 1% for densities between 15-25 g/cm³. At $T = 21.77$ eV, the
623 pressure difference gradually increases from 0 to 1.5% as densities increases from 5 to 12.5
624 g/cm³. The difference further increases to 6% at 25 g/cm³, which suggests that the VASP-
625 PAW frozen-core pseudopotential works well for all densities at low temperatures, and only
626 becomes less reliable at the high temperature of 21.77 eV for densities higher than 12.5 g/cm³
627 at which the core of neighbored atoms overlap. At temperatures of 43.54 and 87.08 eV, the
628 all-electron ONCV pressures are well consistent with PIMC values (differences are within
629 2%).

630 [109] M. A. Meyers, *Dynamic Behavior of Materials* (Wiley, New York, 1994).

631 [110] Our ACTEX calculations are limited to $T > 20$ eV at which point the two-particle contri-
632 bution to the pressure becomes comparable to the Saha term. This is sufficient to capture
633 the peak in the compression on the Hugoniot as well as significant deviation from ideal Saha
634 behavior.

635 [111] X52 is a new Purgatorio-based boron EOS model. It was constructed by following the QEOS
636 approach [9, 10] and decomposing the free energy into contributions from the cold curve,
637 ion-thermal, and electron-thermal parts. The model parameters were constrained by our
638 first-principles EOS data using DFT-MD, PIMC, and ACTEX.

639 [112] See <http://www.msg.ameslab.gov/gamess/> for information about the GAMESS code.

640 [113] Our Purgatorio calculations on boron use the Coulomb potential and the Hedin-
641 Lundqvist [123] form of exchange-correlation functional under local density approximation

- 642 (LDA).
- 643 [114] D. R. Hamann, Phys. Rev. B **88**, 085117 (2013).
- 644 [115] D. R. Hamann, Phys. Rev. B **95**, 239906 (2017).
- 645 [116] A good reference on this can be found in Chap. 3 of the lecture notes by K. Schulten and I.
646 Kosztin: <http://www.ks.uiuc.edu/Services/Class/NSM.pdf>.
- 647 [117] H. D. Whitley, W. E. Alley, W. H. Cabot, J. I. Castor, J. Nilsen, and H. E. DeWitt,
648 Contributions to Plasma Physics **55**, 413 (2015).
- 649 [118] J. D. Kress, J. S. Cohen, D. A. Horner, F. Lambert, and L. A. Collins, Phys. Rev. E **82**,
650 036404 (2010).
- 651 [119] J. Daligault, Phys. Rev. Lett. **96**, 065003 (2006).
- 652 [120] R. M. Darlington, T. L. McAbee, and G. Rodrigue, Comput. Phys. Commun. **135**, 58 (2001).
- 653 [121] B. E. Morgan and J. A. Greenough, Shock Waves **26**, 355 (2016).
- 654 [122] L. H. Yang, R. Q. Hood, J. E. Pask, and J. E. Klepeis, J. Comput.-Aided Mater. Des. **14**,
655 337 (2007).
- 656 [123] L. Hedin and B. I. Lundqvist, J. Phys. C: Solid State Phys. **4**, 2064 (1971).